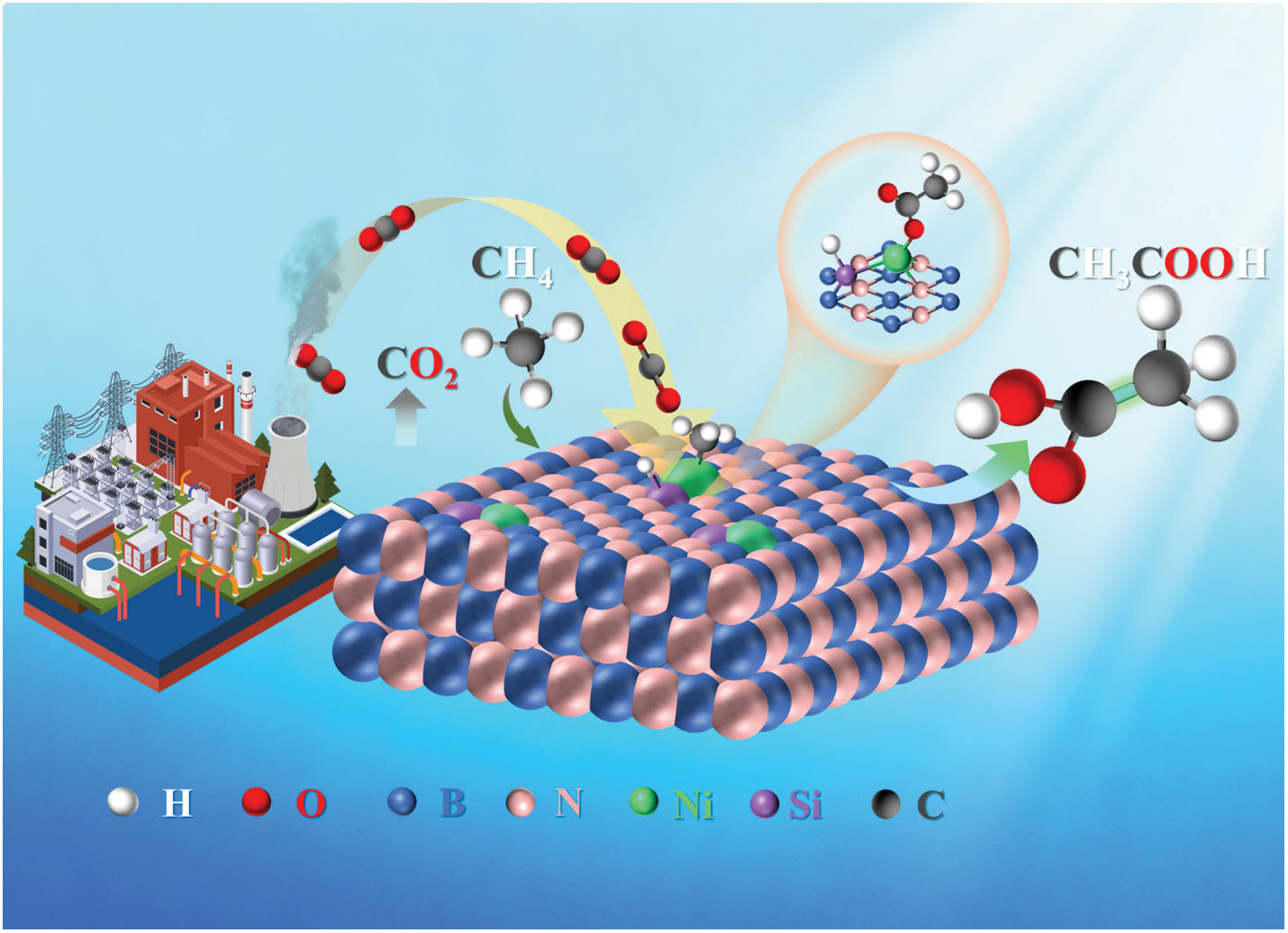

Showcasing research from Professor Haigang Hao's laboratory, College of Chemistry and Chemical Engineering, Inner Mongolia University, China, and Professor Meilan Huang's laboratory, School of Chemistry and Chemical Engineering, Queen's University, UK.

First-principles insights into the direct synthesis of acetic acid from CH_4 and CO_2 over TM–Si@2D catalysts

DFT calculations reveal a TM–Si@2D single-atom catalyst that directly couples CH_4 and CO_2, defining a new paradigm for greenhouse-gas mitigation and the sustainable production of high-value acetic-acid–derived chemicals.

Image reproduced by permission of Haigang Hao from *Chem. Commun.*, 2025, **61**, 19836.

As featured in:

See Haigang Hao, Meilan Huang *et al.*, *Chem. Commun.*, 2025, **61**, 19836.

ROYAL SOCIETY OF CHEMISTRY

rsc.li/chemcomm

Registered charity number: 207890

ChemComm

COMMUNICATION

View Article Online
View Journal | View Issue

Cite this: *Chem. Commun.*, 2025, **61**, 19836

Received 23rd August 2025,
Accepted 27th October 2025

DOI: 10.1039/d5cc04864h

rsc.li/chemcomm

First-principles insights into the direct synthesis of acetic acid from CH_4 and CO_2 over TM–Si@2D catalysts

Mingyuan Zhang,[a] Linxia Cui,[a] Yang Jiang,[a] Rui Gao,[a] Haigang Hao*[a] and Meilan Huang *[b]

The direct synthesis of acetic acid from natural gases has attracted great attention. However, achieving selective C–C coupling remains a major challenge. We designed doped single-atom transition metal catalysts on 2D materials, guided by DFT calculations on the reaction pathways for acetic acid synthesis *via* CH_4/CO_2 coupling. Among the catalysts examined, Ni–Si@h-BN shows strong electron synergy in CH_4 activation and C–C coupling under the E–R mechanism, confirmed by kinetics.

Transforming CH_4 and CO_2 into acetic acid offers a green route to convert greenhouse gases into value-added chemicals.[1] Understanding the reaction mechanism is essential for catalyst design: CH_4 first dissociates into CH_3* and H*, after which CH_3* couples with CO_2 to form CH_3COO*. This intermediate undergoes hydrogenation to yield CH_3COOH, which subsequently desorbs as acetic acid.[2] Homogeneous catalysts like $Pd(OAc)_2/Cu(OAc)_2/K_2S_2O_8/CF_3COOH$,[3] $RhCl_3$[4] and $PdSO_4$[5] have been used for this conversion, but it is challenging to recycle the catalysts. More practical heterogeneous catalysts use supports like TiO_2, Al_2O_3, SiO_2 and zeolites, with active sites such as Zn or Cu.[6] For instance, Cu-K-ZSM-5 zeolite[7] converts CH_4 and CO_2 to acetic acid at 500 °C, achieving 5% CH_4 conversion and 100% acetic acid selectivity after 1 hour, while ZnO–CeO_2 supported on montmorillonite[8] achieves 8.33% CH_4 conversion and 100% selectivity at 300 °C. Zn-based catalysts generally show higher activity than Cu-based ones but they still require stringent conditions for effective activation.[9] Theoretical calculations can underpin experimental efforts to improve catalyst activity by revealing reaction pathways and energy barriers. In particular, understanding the elementary steps of C–H activation and subsequent C–C coupling is especially important for the direct synthesis of acetic acid catalysts.[10] Langmuir–Hinshelwood (L–H) and Eley–Rideal (E–R) mechanisms are two commonly adopted mechanisms for CO_2–CH_3* coupling. Nie *et al.*[11] found that Fe/ZnO_2 catalysts activate CH_4 efficiently due to Fe–Zn bimetallic synergy, with low barriers for CH_4 activation (0.30 eV) and C–C bond formation (0.75 eV) *via* the L–H pathway. However, the L–H mechanism requires dual adsorption sites, which increases the probability of side reactions.[12] The E–R mechanism, involving reactions between gas-phase molecules and adsorbed species, usually reflects experimental conditions.[13] When CH_4 and CO_2 compete for adsorption sites, the relative adsorption strengths govern which pathway becomes dominant. In the Zn-ZSM-5 catalysts,[14] CH_4 preferentially adsorbs on Zn^{2+} sites to form CH_3* intermediates, while CO_2 shows weak affinity (<0.2 eV), and thus gas-phase CO_2 couples directly with adsorbed CH_3 following an E–R mechanism. Although Zn-ZSM-5 lowers the barriers for CH_4 activation (0.65 eV) and acetate formation (0.20 eV), its C–C coupling activity remains limited (1.79 eV), underscoring the need to exploit selective C–C bond formation by other transition metal catalysts under the E–R pathway. Catalysts with well-defined single-site active units[15]—such as isolated metal atoms with specific coordination environments or tailored metal–support interfaces—are highly promising for enhancing C–C coupling *via* the E–R mechanism.

Nickel is commonly used for CH_4 conversion due to its high activity, but it is prone to coking and sintering.[16] Studies show that adding Si atoms in Ni–Si/ZrO_2 catalysts enhances Ni dispersion, stability, and resistance to coking during CH_4 and CO_2 dry reforming.[17] This inspired us to examine the effect of Si on the electron density of Ni-based catalysts, to optimize Ni sites for coupling CH_4 and CO_2 into acetic acid. On the other hand, single-atom catalysts (SACs) on 2D materials have shown significant potential for CO_2 conversion, owing to their high atom utilization and activity, for example, Feng *et al.* demonstrated that SACs embedded in a 2D graphitic carbon nitride support exhibit high catalytic efficiency.[18] For example, Zn-based metal oxide SACs show unique catalytic properties for

[a] *School of Chemistry and Chemical Engineering, Inner Mongolia University, Hohhot, Inner Mongolia 010021, China. E-mail: haohaigang@imu.edu.cn*
[b] *School of Chemistry and Chemical Engineering, Queen's University, Belfast, BT9 5AG, UK. E-mail: m.huang@qub.ac.uk*

converting CH_4 and CO_2 to acetic acid; however, efficient C–C coupling remains a challenge.[19] The high surface area and stability of two-dimensional (2D) materials enable SACs@2D systems with well-defined active centres, surpassing conventional metal oxide supports[20] and potentially improving C–C coupling. Herein, we designed SACs composed of transition metals (Mn, Fe, Co, and Ni) doped with Si promoters on h-BN (TM–Si@h-BN) to identify the optimal active component. Subsequently, we evaluated various 2D materials, including graphene (GR), N_4-doped graphene (N_4@GR), and phosphorene (P), to determine the optimal catalyst configuration. We demonstrated that Ni–Si@h-BN is a promising alternative to traditional catalysts and elucidated its activation and reaction mechanism: electron transfer from Si to Ni creates an electron-rich Ni site ($Ni^{-2.16}$) and its moderate work function is favourable for electron balance, facilitating CH_4 activation and CO_2 adsorption.

The computed binding energy (E_b) and formation energy (E_f)[21] for TM–Si@h-BN catalysts demonstrate the stability of Si and TM atoms on h-BN (Table S1). AIMD simulations of the TM–Si@h-BN catalyst structure at 500 K demonstrate its thermodynamic stability (Fig. S1a and b). Bader charge calculations (Table S1) show electron transfer from Si to transition metals, forming a $TM_1^{\delta-} - Si_1^{\delta+}$ distribution. We compared the adsorption abilities of CH_4 and CO_2 at 500 K. Although both CH_4 and CO_2 exhibit relatively weak interactions with the surfaces, CH_4 binds more strongly (−0.36 to 0.15 eV) than CO_2 (0.22–0.65 eV) on all TM–Si@h-BN catalysts, underscoring that CH_4 is preferentially activated across these materials (Fig. S1c and d). The work function (Fig. S2), reflecting the electron transfer ability of TM–Si@h-BN, controls CH_4 and CO_2 adsorption such that CH_4 adsorption weakens with increasing work function, while CO_2 adsorption strengthens (Fig. S3a).

The dissociation of CH_3* at TM sites is influenced by the presence of doped Si. On Mn–Si@h-BN and Fe–Si@h-BN, the H atom is co-adsorbed with CH_3* on the top site of TM, exhibiting low energy barriers of 0.27 and 0.44 eV (Fig. 1 and Table S4), respectively. On Co–Si@h-BN, H* prefers the Co–Si bridge site, with a higher barrier of 0.96 eV. On Ni–Si@h-BN, the hydrogen atom migrates to the top site of Si, incurring an energy barrier of 0.50 eV. The C–C coupling is initiated by the reaction of CH_3* and gaseous CO_2, forming the CH_3COO* intermediate at TM sites *via* the E–R mechanism. Ni–Si@h-BN shows the lowest barrier for this step (0.71 eV) among the TM–Si@h-BN catalysts, and crystal Hamilton population (COHP) analysis reveals a weaker Ni–CH_3 bond (integrated strength ICOHP: −1.18 eV) that facilitates CO_2 insertion (Fig. S7). The hydrogenation of CH_3COO* to acetic acid generally proceeds with high barriers on TM–Si@h-BN. Furthermore, the energetic span model (δE) was employed as a direct descriptor of the catalytic cycle rate.[22] At 500 K, except for Mn–Si, where TS3 (CH_3COO* hydrogenation) is the turnover-determining transition state (TDTS), TS2 (C–C coupling) serves as the TDTS for the other TM–Si systems, while CH_3COO* + H* acts as the turnover-determining intermediate (TDI) in all cases. The corresponding δE values for each system are summarized in Table S12. Notably, Ni–Si@h-BN shows the lowest δE (1.26 eV), emphasizing its superior activity and highlighting its potential as a 2D support for further optimization.

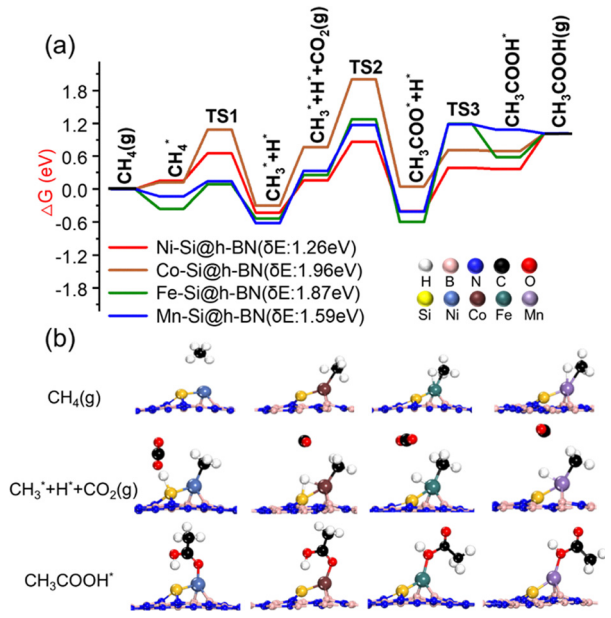

Fig. 1 The coupling of CH_4 and CO_2 into acetic acid on TM–Si@h-BN at 500 K. (a) Reaction energy profile (energy span, δE is shown in parentheses). (b) Adsorption configurations of key reactants and products. See Fig. S6 and Table S4 for details.

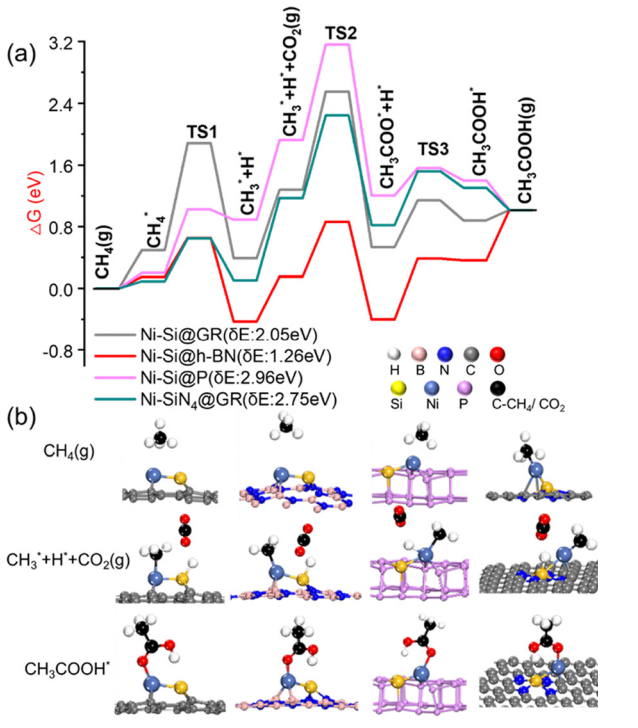

Fig. 2 The coupling of CH_4 and CO_2 into acetic acid on Ni–Si@2D at 500 K. (a) Reaction energy profile (energy span, δE is shown in parentheses). (b) Adsorption configurations of key reactants and products. See Fig. S9 and Table S9 for details.

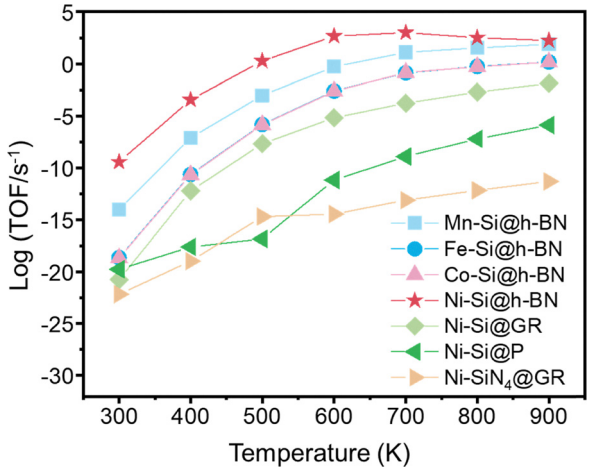

Fig. 3 Turnover frequencies for CH_3COOH production over TM–Si@2D as a function of temperature (CH_4/CO_2 = 1 : 1, 1 bar).

The structural stability of Ni–Si@2D and the thermodynamic stability of Ni–Si@2D at 500 K are confirmed (Fig. S8). Bader charge analysis reveals that silicon donates electrons to transition metals on both Ni–Si@2D and TM–Si@h-BN catalysts, highlighting its general role as an electron donor (Table S5), and accounting for the stronger CH_4 adsorption observed on TM–Si@2D compared to TM@2D (Table S7).

The CH_4 adsorption energy on Ni–Si@2D strengthens with increasing work function, whereas the CO_2 adsorption energy exhibits a volcano-shaped trend (Fig. S3b). The Ni atom in Ni–Si@2D was identified as the primary activation site for CH_4 dissociation (Fig. 2 and Table S9), with Ni–Si@h-BN exhibiting the lowest barrier (0.50 eV), outperforming Ni–Si@GR, Ni–Si@P, and Ni–SiN_4@GR. The Bader charge analysis of the C–C coupling step (Table S10) reveals that electrons transfer from the CH_3–TM bond to CO_2, facilitating C–C bond formation. Ni–Si@h-BN exhibits a barrier of 0.71 eV for C–C coupling, which is comparable to other Ni–Si@2D systems and lower than the reported E–R pathway catalysts.[19] During acetic acid formation and desorption, most hydrogenation reactions proceed easily on Ni–Si@2D. For Ni–Si@2D catalysts at 500 K, the energy span is smallest on h-BN (1.26 eV), indicating its superior activity. While TS2 (C–C coupling) is the TDTS across all systems, the TDI differs: it is $CH_3COO^* + H^*$ on Ni–Si@h-BN whereas it is adsorbed CH_4^* on the others. Together with fast CH_4 dissociation, facile C–C coupling, and favourable hydrogenation, Ni–Si@h-BN exhibits markedly enhanced activity compared with other reported catalysts (Table S11). By-product formation during acetic acid synthesis on Ni–Si@h-BN was also evaluated. Energetic span analysis shows that the C–C coupling pathway to CH_3COO^* (δE = 0.71 eV) is much more favorable than CO_2 hydrogenation routes *via* COOH or HCOO (δE = 1.97 and 0.81 eV), indicating that C–C coupling dominates over formic acid formation (Fig. S12).

To further understand temperature effects, the energetic span was analysed at different temperatures, and the corresponding TDTS and TDI are summarized in Table S12. Ni–Si@h-BN exhibits the lowest δE across 300–900 K, reaching 1.23 eV at 600 K (Fig. S13). Based on the energetic span model, the TOFs for acetic acid formation (300–900 K, 1 bar)[23] were calculated (Fig. 3), showing consistently high TOFs for Ni–Si@h-BN, with a peak at 700 K (8.02×10^{-2} s^{-1}, log TOF: 2.90), after which the TOFs decrease with further temperature increase. These results highlight Ni–Si@h-BN as an efficient catalyst for CH_4 and CO_2 conversion under moderate conditions while minimizing coke formation.[24]

Understanding the relationship between catalytic performance and electronic properties is crucial for designing new

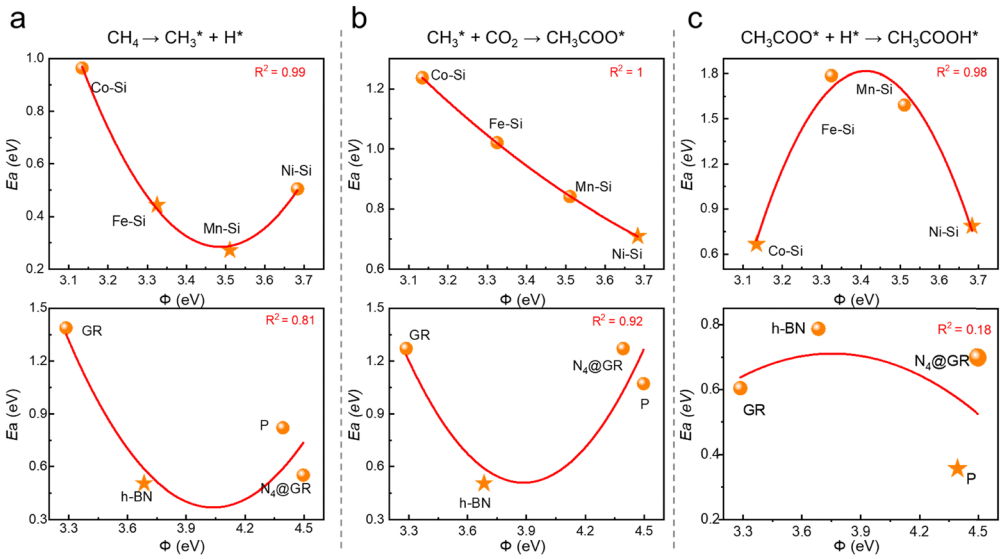

Fig. 4 Relationship between work function (ϕ) and energy barriers (E_a) for acetic acid synthesis from CH_4 and CO_2 on TM–Si@2D at 500 K: (a) CH_4 dissociation; (b) C–C coupling; (c) acetic acid formation. Upper panel: The 2D material is h-BN, lower panel: the transition metal is Ni–Si on different 2D materials.

catalysts for efficient CH_4–CO_2 coupling toward acetic acid. CH_4 dehydrogenation on TM–Si@2D exhibits a volcano dependence on work function (Fig. 4a), with the lowest barriers with moderate values (3.3–4.0 eV) due to optimal polarization of the C–H bond. For C–C coupling (Fig. 4b), most TM–Si@2D follows a volcano-like behaviour, whereas TM–Si@h-BN shows a nearly linear decrease in barrier with increasing work function, benefiting from π back-donation that enhances CO_2 adsorption and facilitates CH_3* activation. In contrast, CH_3COO hydrogenation follows an inverse volcano relationship to the work function (Fig. 4c), showing reduced barriers at both low and high work function values. Bader charge analysis (Fig. S14) further confirms that higher TM electron density generally is attributed to reduced barriers throughout the entire reaction process. Ni–Si@h-BN, characterized by an electron-rich Ni site ($Ni^{-2.16}$) and a moderate work function (3.68 eV), exhibits the lowest barrier in the rate-determining step and thus maintains thermodynamic favourability across all three elementary steps. This results from its balanced electron donation to the substrate with optimal adsorption strength.

We elucidated the acetic acid synthesis mechanism from CO_2 and CH_4 and designed TM–Si@2D based on DFT calculations. Silicon incorporation enriches transition metals with electrons, generating electron-rich active sites that enhance the catalytic activity. Ni–Si@h-BN stands out among doped transition metal catalysts. Its moderate work function and high Ni electron density facilitate CH_4 activation, while the $TM_1^{\delta-}$ – $Si_1^{\delta+}$ synergy enables C–C coupling through the E–R mechanism. The turnover frequency for CH_4 and CO_2 conversion to acetic acid reaches 8.02×10^{-2} s^{-1} at 700 K and 1 bar, demonstrating the reaction's feasibility under practical conditions. This advantageous electronic structure underpins its capability for efficient and selective acetic acid synthesis.

This study was supported by the National Natural Science Foundation of China (No. 22172083, 22462020), the 111 Project (D20033), Inner Mongolia Science and Technology Planning Programme (2025YFKL0002). We also acknowledge Inner Mongolia China HPC Technology Co. LTD and Kelvin2 from NI-HPC at Queen's University Belfast for its Super-Server for the DFT calculations.

Conflicts of interest

There are no conflicts to declare.

Data availability

The data supporting this article have been included as part of the supplementary information (SI). Supplementary information is available including computational details, adsorption energies and work function, binding energies, Bader charges, activation energies, reaction energies, the structures and key geometry parameters of the reaction states. by product formation pathways, and energy spans calculated at different temperatures. See DOI: https://doi.org/10.1039/d5cc04864h.

Notes and references

1 (*a*) Y. Li, K. Zheng, Y. Shen, M. Huang, B. Liu, Y. Xu and X. Liu, *J. Phys. Chem. C*, 2023, **127**, 5841–5854; (*b*) B.-S. Mu, Y. Zhang, M. Peng, Z. Tu, Z. Guo, S. Shen, Y. Xu, W. Liang, X. Wang, M. Wang, D. Ma and Z. Liu, *Angew. Chem., Int. Ed.*, 2024, **63**, e202407443.
2 X. Zan, S. Tao, C. Zhang, Y. Wu, Y. Liu and W. Huang, *J. Energy Inst.*, 2024, **116**, 101739.
3 Y. Fujiwara, Y. Taniguchi and K. Takaki, *Stud. Surf. Sci. Catal.*, 1997, **107**, 275–278.
4 I. H. Hristov and T. Ziegler, *Organometallics*, 2003, **22**, 3513–3525.
5 S. Chempath and A. T. Bell, *J. Am. Chem. Soc.*, 2006, **128**, 4650–4657.
6 (*a*) Z. Riguang and B. W. Wei H, *Chin. J. Catal.*, 2008, **29**, 913; (*b*) Y. Liu, N. Cui, P. Jia and W. Huang, *Catalysts*, 2020, **10**, 131; (*c*) N. Shahzad and B. Khan, *J. Mol. Graphics Modell.*, 2021, **105**, 107896.
7 A. M. Rabie, M. A. Betiha and S. E. Park, *Appl. Catal., B*, 2017, **215**, 50–59.
8 R. Shavi, J. Ko, A. Cho and J. W. Han, *Appl. Catal., B*, 2018, **229**, 237–248.
9 (*a*) J. Chen, W. Xu and H. Zhang, *ACS Appl. Nano Mater.*, 2024, **7**, 11285–11294; (*b*) N. Liu, N. Lu and K. Zhao, *Chem. Eng. J.*, 2024, **487**, 150690.
10 C. Tu, X. Nie and J. G. Chen, *ACS Catal.*, 2021, **11**, 3472–3482.
11 X. Nie, X. Ren and C. Tu, *Chem. Commun.*, 2020, **56**, 3983–3986.
12 (*a*) C. Liu, X. Li and Y. Wang, *ChemCatChem*, 2016, **8**, 421–433.; (*b*) B. Hu, H. Yang and Y. Luo, *J. Catal.*, 2019, **369**, 331–343.; (*c*) H. Wu, A. Singh-Morgan and K. Qi, *ACS Catal.*, 2023, **13**, 5375–5396; (*d*) L. Zhu, Y. Lin and K. Liu, *Chin. J. Catal.*, 2021, **42**, 1500–1508.
13 (*a*) Y. Wang, G. Wu, M. Yang and J. Wang, *J. Phys. Chem. C*, 2013, **117**, 8767–8773; (*b*) D. Kiani and I. E. Wachs, *ACS Catal.*, 2024, **14**, 16770–16784.
14 M. H. Mahyuddin, S. Tanaka and Y. Shiota, *Bull. Chem. Soc. Jpn.*, 2020, **93**, 345–354.
15 (*a*) D. Kiani and I. E. Wachs, *ACS Catal.*, 2024, **14**, 16770–16784; (*b*) J. Wang, Q. Song, Y. Shang, Y. Liu and J. Zhao, *Nanomaterials*, 2023, **15**, 1111.
16 (*a*) R. Benrabaa, A. Löfberg and A. Rubbens, *Catal. Today*, 2013, **203**, 188–195; (*b*) J. Niu, J. Ran and D. Chen, *Appl. Surf. Sci.*, 2020, **513**, 145840; (*c*) J. Li, E. Croiset and L. Ricardez-Sandoval, *Appl. Surf. Sci.*, 2014, **311**, 435–442.
17 (*a*) Y. Wang, L. Yao and Y. Wang, *ACS Catal.*, 2018, **8**, 6495–6506; (*b*) L. Li, Y. Wang and Q. Zhao, *Catalysts*, 2021, **11**, 1–14.
18 (*a*) J. Feng, H. Gao and L. Zheng, *Nat. Commun.*, 2020, **11**, 1–8; (*b*) J. Yuan, W. Zhang and X. Li, *Chem. Commun.*, 2018, **54**, 2284–2287; (*c*) K. Homlamai, T. Maihom and S. Choomwattana, *Appl. Surf. Sci.*, 2020, **499**, 143928.
19 (*a*) P. Zhang, X. Yang and X. Hou, *Catal. Sci. Technol.*, 2019, **9**, 6297–6307; (*b*) R. Li, J. Wu and X. Zhao, *Chem. Eng. J.*, 2024, **490**, 151528.
20 (*a*) J. M. Zamalloa-Serrano, J. I. Mendieta-Moreno and J. M. Gómez-Fernández, *Carbon*, 2024, **229**, 119544; (*b*) Y. Cheng and J. Zhou, *iScience*, 2024, **27**, 108788.
21 L. Cui, K. Shi and M. Zhang, *Fuel*, 2023, **340**, 127541.
22 (*a*) S. Kozuch and S. Shaik, *Acc. Chem. Res.*, 2011, **44**, 101–110; (*b*) J. Chen, Y. Chen, P. Li, Z. Wen and S. Chen, *ACS Catal.*, 2018, **8**, 10590–10598.
23 (*a*) Y. Zhao, H. Wang, J. Han, X. Zhu, D. Mei and Q. Ge, *ACS Catal.*, 2019, **9**, 3187–3197; (*b*) A. M. Rabie, M. M. Hassan, E. A. El-Sharkawy and A. E. Awadallah, *Appl. Catal., B*, 2017, **215**, 50–59; (*c*) M. G. Sibi, S. Chandran, R. C. Devarajan and N. R. Shiju, *ACS Catal.*, 2021, **11**, 8382–8398.
24 (*a*) L. He, M. Li, W.-C. Li, W. Xu, Y. Wang, Y.-B. Wang, W. Shen and A.-H. Lu, *ACS Catal.*, 2021, **11**, 12409–12416; (*b*) J. W. Han, C. Kim, J. S. Park and H. Lee, *ChemSusChem*, 2014, **7**, 451–456.